## MATERIALS SCIENCE

# Geological timescales' aging effects of lunar glasses

Ziqiang Chen[1]†, Yong Zhao[1]†, Xiang Chi[1], Yuqiang Yan[1], Jie Shen[2], Minjie Zou[1], Shaofan Zhao[3], Ming Liu[3], Wei Yao[3], Bo Zhang[1]*, Haibo Ke[1]*, Xiu-Liang Ma[1,2], Haiyang Bai[1,2,3]*, Mengfei Yang[3], Zhigang Zou[3,4], Wei-Hua Wang[1,2,3]

Physical aging is a long-lasting research hot spot in the glass community, yet its long-term effects remain unclear because of the limited experimental time. In this study, we discover the extraordinary aging effects in five typical lunar glassy particles with diameters ranging from about 20 to 53 micrometers selected from Chang'e-5 lunar regolith. It is found that geological time scales' aging can lead to unusually huge modulus enhancements larger than 73.5% while much weaker effects on hardness (i.e., varies decoupling evolutions of Young's modulus and hardness during aging) in these lunar glassy samples. Such extraordinary aging effects are primarily attributed to the natural selected complex glassy compositions and structures, consistent with high entropy and minor element doping criteria, prevailing under the special lunar conditions and the extensive aging time for the lunar glasses. This study offers valuable insights for developing high-performance and stable glassy materials for radiation protection and advanced space explorations.

## INTRODUCTION

Glass has been regarded as the fourth state of conventional matters besides gas, liquid, and solid (1) and is one of the most vital and influential materials for the development of human society (2). Nowadays, glasses have become necessities in our daily lives, used as mirrors, windows, screens, cutting tools, containers, adornments, lamps, fibers, etc. With the progress of modern civilization, the demand for advanced glasses is increasing day by day to cope with the global challenges from the environment and energy to health care and information technology (3). Therefore, it is of great importance to clarify the relationship between the structure and properties of glasses and thus provide guidance for the development of high-performance glasses.

Glass is generally in thermodynamic nonequilibrium because of the preparation method of fast cooling, which introduces the quenched-in structural defects. As a result, physical aging (or structural relaxation) inevitably occurs below the glass transition temperature ($T_g$), driving glass toward a lower energy state with the time evolution. Physical aging causes the structure and properties of glass to evolve with time (4), and these effects directly influence the stability of glass. This makes physical aging a long-lasting research hot spot in the glass community. For instance, it will cause the brittle glasses to become even more brittle, which directly affects their service security and prevents them from being widely used as structural materials (4). In particular, the long-term aging effects of glass attract key focus because they may determine the lower limit of the energy state and the corresponding limit of structure and property of glass. Related works showed various or even controversial results. For instance, Zanotto (5), as well as Gulbiten et al. (6), demonstrated by numeric calculations that the stained-

glass windows can hardly flow at room temperature (RT) in a human time scale and the related famous urban legend that the glass windows in medieval cathedrals are thicker in the lower parts might be a rumor. Pérez-Castañeda et al. (7) reported the hyperstability of two-level systems and boson peak in the amber glass even after 110 million years of aging. Meanwhile, Welch et al. (8) showed that 1.5 years of RT aging produced a measurable shrinkage in the Corning Gorilla Glass. For another, it was reported that ultrastable organic glasses (9), polymer glasses (10), and metallic glasses (MGs) (11) could be prepared by vapor depositions, which have properties similar to those thermally expected after aging the corresponding ordinary glass for hundreds to thousands of years. Recently, our group (12) demonstrated that a Ce-based MG approached a much more stable state without crystallization after 17.7 years of RT aging. However, because of the very limited experimental time or the very limited glass variety that have aged for enough long time, the long-term aging effects of glasses have not yet been well clarified.

Lunar glasses, which are a common component in lunar regolith, originate mainly from meteorite impacts (13). They have experienced extremely long time scale's weathering and aging (about millions to billions of years) but maintained the glassy nature (14, 15). As weathering mainly affects the surface region (~100 to 200 nm) of lunar glasses (16), the inner part of lunar glasses could be the ideal model to evaluate the long-term aging effects of glasses. For another, the glass content (mainly including glassy particles and agglutinates) in the lunar regolith generally increases as its maturity (indicates how long a grain has been exposed at the surface) increases, and it is up to ~60 to 70% volume fraction in some highly mature Apollo lunar regolith (17, 18), indicating that glass (or glassy state) might be the most suitable and stable material (or structural state) in space environment. It is in line with the experimental results that glassy materials have better irradiation resistance and comparable overall mechanical properties relative to their crystalline counterparts (19). Meanwhile, glass is also a common component of the regolith for many other planets, such as Mars, Mercury, and Venus, and large asteroids (20). Thence, glassy materials have great application potentials in space exploration. As lunar regolith

[1]Songshan Lake Materials Laboratory, Dongguan 523808, China. [2]Institute of Physics, Chinese Academy of Sciences, Beijing 100190, China. [3]Qian Xuesen Laboratory of Space Technology, China Academy of Space Technology (CAST), Beijing 100094, China. [4]College of Engineering and Applied Sciences, Nanjing University, Nanjing 210093, China.
*Corresponding author. Email: zhangbo@sslab.org.cn (B.Z.); kehaibo@sslab.org.cn (H.K.); hybai@iphy.ac.cn (H.B.)
†These authors contributed equally to this work.

provides the most economical and convenient raw materials for space exploration, glassy materials made from lunar regolith should be given priority. Therefore, clarifying the aging effects of lunar glasses, which have similar chemical compositions to the local regolith (*13*, *15*), is of great importance for the material selection and design of future lunar and interplanetary explorations. Moreover, studies on the aging effects of the natural chosen lunar glasses, which have rather complex chemical composition [major elements such as O, Si, Fe, Mg, Al, Ca, and Ti, as well as some other minor elements such as Na, K, S, etc. (*13*)] may also shed light on the understanding of the physical aging of multicomponent glassy materials such as MGs and high-entropy (HE) glasses, hence beneficial for material design and property control of these newly developed materials.

In this work, five typical glassy particles with relatively large size were intentionally selected from the lunar regolith returned by Chang'e-5. These particles include four spherules with diameters ranging from 20 to 53 μm and one ellipsoid of similar size. The five particles, referred to as particles I to V were chosen so that their extreme long-term aging effects can be studied. As the glassy particles are very small [note that almost all glassy particles in the lunar regolith of Chang'e-5 are less than dozens of micrometers in diameter (*17*)], we quantitatively evaluate their aging effects by transmission electron microscopy (TEM) observation and nanoindentation tests [a common micro- and nanomechanical testing method (*21*)] rather than the traditional thermal methods. The examined samples are all cut from the inner part of the glassy particles to eliminate the effects of weathering. Note that the fresh glassy particles (i.e., the initially formed glass particles by impacting) can hardly be obtained by the available instruments, as they were derived from the micrometeorites impacting the moon with fast cooling rates [hundreds to thousands of Kelvins per second (*22*, *23*)]. Here, we create some rejuvenated samples for these glassy particles, which are taken as the reference samples to partially evaluate their aging effects, by heating the hyperaged (H-A) ones (i.e., the returned glassy particles that have experienced weathering and aging over extremely long time) up to the supercooled liquid region, holding for 60 s, and then cooling down to RT at relatively lower cooling rates. Theoretically, as the structure and energy state of each rejuvenated sample lies between the corresponding fresh one and the H-A one, as shown in Fig. 1, it is rational to partially evaluate the aging effects of each lunar glassy particle by using the rejuvenated sample as the reference one. Moreover, to experimentally verify the rationality of such partial evaluation method, apart from the lower cooling rate (~40 K/min) applied for all the glassy particles, a higher cooling rate (~240 K/s) was additionally applied for glassy particles IV and V. The samples obtained by the lower cooling rate and the higher cooling rate are termed as less-rejuvenated (L-R) one and more-rejuvenated (M-R) one, respectively. It is found that the very long-term aging effects of lunar glasses, although composition dependent, are generally very remarkable. Particularly, the partially evaluated aging-induced increments of Young's modulus are as high as dozens of percentages in these lunar glassy particles, which is hardly reported before in other glasses. Moreover, various degrees of decouplings between the Young's modulus and hardness are observed in these glassy particles. The study delves into the underlying mechanisms behind the peculiar aging-induced increments of Young's modulus and the decoupling of changes in Young's modulus and hardness in lunar glasses. This work also provides valuable insights and a comprehensive guideline for the design of innovative high-performance glassy materials with adjustable mechanical properties.

## RESULTS
### Thermal properties of lunar glasses

We first conducted thermal analysis with two successive heating runs for the lunar regolith to determine the thermodynamic characteristic signals [such as $T_g$ and crystallization temperature ($T_x$)] and the relative content of the lunar glasses. A spoon of lunar regolith of ~20 mg was weighed for thermal analysis. As shown in Fig. 2A, in the first heating curve, $T_g$ and $T_x$ of the measured lunar regolith were 936 and 1030 K, respectively. The measured vitrification, crystallization, and melting temperatures are consistent with those previously reported in other lunar regolith samples (*23*). In the second heating curve, a pronounced vitrification signal ($T_g$ = 935 K) is followed by a sharp crystallization exothermic event ($T_x$ = 1083 K) and a much weaker melting endothermic peak. The glass transition in the second heating curve originates from the complete vitrification of the lunar regolith after melting and quenching in the first heating run. The glass nature of lunar regolith in the second heating run is demonstrated in fig. S1. Note that the crystallization enthalpy ratio between that in the first heating run (partially vitrified of 28.8 J/g) and that in the second heating run (completely vitrified of 180.5 J/g) is ~16.0%, which is in line with the glass phase fraction in the lunar regolith of Chang'e-5 [~16.6 wt % (*17*) and 15.5 wt % (*24*)]. This result confirms that the vitrification and crystallization signals observed in the first heating curve originate from the lunar glasses contained in the lunar regolith.

Furthermore, to study the geological time scales' aging effects on the thermal properties of the lunar glasses, a new spoon of original lunar regolith sample (~20 mg) was only heated to 973 K in the supercooled liquid region at 40 K/min, held for 60 s, and then cooled down to RT at 40 K/min under a purified argon atmosphere, thus erasing the thermal history of the H-A glasses to obtain the L-R sample with the same composition (an identical procedure as the obtainment of the L-R glassy particles). As shown in Fig. 2B, $T_g$ of the L-R sample was measured to be 928 K, which is 8 K lower than that of the corresponding H-A sample (936 K). The increase of $T_g$ ($\Delta T$) in lunar glasses upon aging suggests an enhanced kinetic stability, as higher temperatures are required to dislodge the atoms from the trapped glassy configuration into a mobile equilibrium supercooled liquid. It is in line with the results of previous studies that the H-A glass had a higher $T_g$ than the corresponding fresh or rejuvenated one (*11*, *12*, *25*). Meanwhile, the H-A sample exhibits a more pronounced endotherm in the proximity of the glass transition with respect to the L-R one, as illustrated in the inset of Fig. 2, indicating that the H-A sample is in a lower thermodynamic energy state compared to the L-R one. Note that the $\Delta T$ of 8 K and the endothermic discrepancy in the proximity of the glass transition between the H-A sample and L-R one correspond to the partially evaluated average aging effects of the whole lunar glasses rather than to any individual lunar glassy particle. According to the mechanical results in the later part, it can be expected that $\Delta T$ and the enhancement of endotherm in the proximity of the glass transition between the H-A sample and M-R one could be larger than those observed in Fig. 2B. However, we cannot obtain the M-R sample for the whole lunar glasses as the higher cooling rate can be only
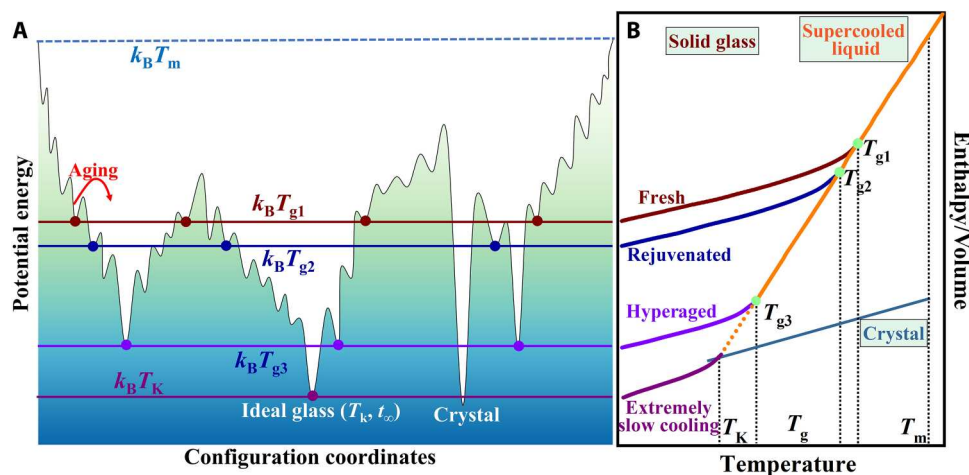
**Fig. 1. Schematic diagram of the structure and energy state of glasses by different cooling rate.** (**A**) Potential energy landscape showing relaxation processes in glasses. (**B**) Change in volume or enthalpy of the supercooled liquid during the thermal process at constant pressure. In this study, the fresh sample indicates the initially formed glass particle by impacting with fast cooling rate; the H-A sample means the returned glassy particle that have experienced weathering and aging over an extremely long time; and the rejuvenated sample indicates the glassy particle obtained by heating the H-A one up to the supercooled liquid region, holding for 60 s, and then cooling down to RT at relatively lower cooling rate. As the volume and energy state of glass are proportional to the cooling rate, the structure and energy state of the rejuvenated sample lies between the corresponding fresh one and the H-A one. In the hypothetical scenario where a supercooled liquid can infinitely supercool at an extremely slow rate, the supercooled liquid will be frozen into a glass at a certain temperature $T_K$ (Kauzmann temperature) above absolute zero, undergoing a glass transition. $T_K$ represents the lowest temperature point at which a liquid undergoes the glass transition. The glass transition occurring at $T_K$ is considered as the thermodynamic idealization of the glass transition, resulting in the formation of an idealized glass for amorphous materials.

achieved by flowing gas, which is not suitable for our powder sample.

As the lunar glasses are very fine and mixed with the crystalline minerals, it is inoperable to isolate enough pure glass samples from the lunar regolith for more elaborately thermal analysis. Moreover, from the heat flow curve of the entire lunar regolith, it is hard to precisely extract the key characteristics [such as sub-$T_g$ endothermic peak, the specific heat step at $T_g$, and the fictive temperature ($T_f$) (26, 27)] of lunar glasses for traditional thermal analysis, as the baseline signal of the heat flow for the crystalline components of lunar regolith is too strong. Therefore, to study the aging effects of lunar glasses more accurately, we intentionally selected five typical glassy particles (termed as particles I to V) with relatively large sizes for TEM observation and nanoindentation tests. The determination of $T_g$ and $T_x$ of lunar glasses in Fig. 2A provides a basis for the subsequent rejuvenation treatment for these glassy particles.

## Morphologies and compositions of the lunar glassy particles

In these five glassy particles, one is a partial ellipsoid (particle II) with an equivalent diameter of ~28 μm, and the remaining four are spherules including particle I with a diameter of ~53 μm, particle III with a diameter of ~20 μm, particle IV with a diameter of ~26 μm, and particle V with a diameter of ~22 μm, as shown in fig. S2 (A to E). The energy-dispersive spectrometry (EDS) spectra indicate that the main constituent elements of these glassy particles are O, Si, Fe, Ca, Al, Mg, and Ti from the perspective of geological science. Glassy particle I contains the minor element Na, and glassy particles II and IV contain the minor element K. The specific compositions of these five particles are listed in table S1, where the concentrations of $SiO_2$, FeO, CaO, $Al_2O_3$, MgO, and $TiO_2$ are ~37.10 to 60.31 wt % [~40.22 to 65.25 atomic % (at %)], ~9.12 to

28.53 wt % (~8.22 to 25.20 at %), ~4.81 to 19.43 wt % (~5.57 to 22.57 at %), ~7.58 to 17.71 wt % (~4.72 to 11.27 at %), ~2.75 to 12.24 wt % (~4.47 to 18.64 at %), and ~1.31 to 6.32 wt % (~1.05 to 5.14 at %), respectively. According to the specific geochemical criteria [i.e., the ratios of $MgO/Al_2O_3$ (28) and $CaO/Al_2O_3$ (29)], all the five glassy particles belong to impact glass with $MgO/Al_2O_3$ ratios <1.25, and particle IV originates from highland (with $CaO/Al_2O_3$ ratio <0.75), while the other four originate from mare (with $CaO/Al_2O_3$ ratios >0.75), as shown in fig. S3.

## Aging condition and time scales

The mean surface temperature of the moon cycles from 120 to 380 K during a month-long lunar day (30). Although it has been reported that fast temperature cycling with a period of several minutes can lead to rejuvenation in some MGs (31); the slow temperature cycling with a period of about 655 hours on the moon should not have such rejuvenation effect. Therefore, the lunar glassy particles were aged at cycling temperature between 120 and 380 K (i.e., $0.13T_g$ to $0.41T_g$).

Moreover, the lunar glassy particles should have experienced long-lasting radiation by solar wind, solar flares, and galactic cosmic rays (30), as the lunar regolith of Chang'e-5 have a high maturity (17). Note that the unusually low glass content in the mature lunar regolith of Chang'e-5 should be attributed to the relatively gentle impact environment (32). Generally, they were mainly affected by the solar wind (made up of ~90% proton, 7% α particle, and very few other elements), which has a much higher flux with a lower energy (~1 KeV/u), with a characteristic penetration distance of a few tens of nanometers (33). Therefore, like many other lunar soil particles reported before (16, 34), a radiation-induced rim with a thickness of ~60 nm formed on the surface of glassy particle I because the rim has identical constituent elements with the inner
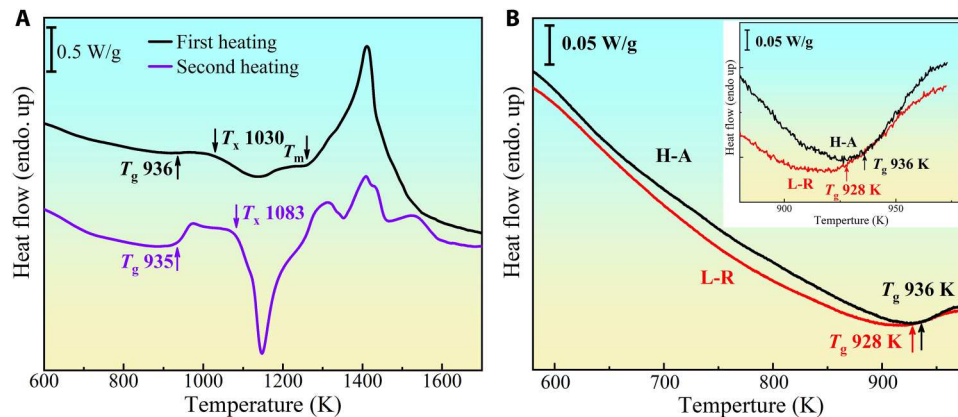
**Fig. 2. Heat flow curves of a spoon of lunar regolith of ~20 mg.** (**A**) The original sample was first heated to 1723 K to ensure complete melting and then cooled to RT in a furnace (black curve). It was then heated for a second time at the same heating rate of 40 K/min (purple curve). (**B**) The original sample of a new spoon of lunar regolith was first heated to 973 K in the supercooled liquid region (black curve), held for 60 s, and then cooled down to RT, thus erasing the thermal history of the H-A lunar glasses to obtain the L-R sample. It was then heated to 973 K for a second time at the same heating rate of 40 K/min (red curve).

part (*16*), as shown in fig. S4. Radiation-induced defects and nano-crystals ($Fe^0$) formed in the rim. Moreover, rare gases might be also injected in the rim. Therefore, to eliminate the effects of solar wind, the examined samples were cut from the inner parts of the glassy particles (more than 10 μm away from the surface), where the solar wind can hardly reach, as we mentioned in the last paragraph of Introduction. Solar flares and galactic cosmic rays (protons, neutrons and heavy particles) with a much lower flux but higher energy (from <1 MeV/u to >100 MeV/u) have a characteristic penetration distance from millimeters to meters (*30*). They would alter the structure of the inner parts of the glassy particles. Glass may undergo aging, rejuvenation, or even crystallization upon irradiation, depending on both the glass (composition, structural, and energy states) and irradiation conditions (particle type, particle energy, particle dosage, and temperature) (*35*, *36*). Generally, apart from crystallization, low dose and low energy irradiation may lead to aging in the high-energy glasses, while high dose and high energy irradiation will result in rejuvenation in the low-energy glasses (*36*–*38*). Therefore, at the very early stage, the lunar glassy particles in a high energy stage will relax toward a lower energy state upon irradiation, i.e., the irradiation ages them and reduces their structural defects in this stage. Then, when the energies of the lunar glassy particles reach a much lower level, irradiation may rejuvenate them to some extent and increases their structural defects. After that, the lunar glassy particles will tend to an equilibrium state at which irradiation-induced defects was balanced by the thermal-reduced defects.

Third, the lunar glassy particles should be also directly or indirectly affected by the micrometeorite impacts, which will generate both mechanical and thermal effects (*39*). In addition, apart from crystallization, it may generate aging or rejuvenation effects on the lunar glassy particles, depending on both the glasses and impact conditions. Therefore, the examined aging effects in these lunar glassy particles should be the complex combined effects of thermal, mechanical, and irradiation factors on the moon under the weathering condition.

Ideally, the age of the lunar glassy particles should be examined via radioisotope dating. However, radioisotope dating can hardly be carried out in these lunar glassy particles, as their sizes are too small

(*40*). Alternatively, the exposure age of the glassy particles can be estimated according to the statistical relationship between the thickness of the radiation-induced rim and the exposure age of the lunar soils (*41*). To reserve enough samples for the subsequent multi-round mechanical tests and structural characterizations, we can only fabricate the outer cross-sectional samples of particles I and II with relatively large sizes and examine their radiation-induced rim. As shown in fig. S4, the rims for both glassy particles I and II originated from solar wind irradiation, as they have identical constituent elements with the inner part of the glassy particles (*16*). The thickness for both rims is ~60 nm, which might be roughly corresponding to an exposure age of ~2 million years (*16*). Therefore, the aging time of these two glassy particles should be more than 2 million years. In view of the result that the thickness is also ~60 nm for the radiation-induced amorphous rim in a recently examined plagioclase particle in the same regolith of Chang'e-5, it can be speculated that most particles in these mature lunar regolith of Chang'e-5 may have the same exposure time of ~2 million years. On the other hand, according to the recent results, the aging time of the lunar glasses of Chang'e-5 should be no more than 2 billion years (*42*, *43*). Therefore, the aging time of these glassy particles of Chang'e-5 might be in the range of 2 million to 2 billion years. It is in line with a very recent result that the age of the examined 215 lunar glassy beads of Chang'e-5 varies from 4 million years to 2 billion years (*14*). Therefore, it qualitatively proves that these five lunar glassy particles should have aged for millions to billions of years.

## Mechanical property change and structural evolution of the lunar glassy particles

Figure 3A shows the relative changes of the reduced Young's modulus ($E_r$) and hardness ($H$) between the H-A sample and the rejuvenated one(s) of the glassy particles. It can be seen that, although the H-A sample has higher $E_r$ and $H$ than the rejuvenated sample for all the glassy particles, the increments of $E_r$ and $H$ between the rejuvenated sample and H-A sample are diverse. Particularly, the increment of $E_r$ between the L-R sample and the H-A one is most notable for particle I of 66.4% and followed by particle IV of 38.3%, particle II of 34.0%, particle III of 11.0%, and particle V
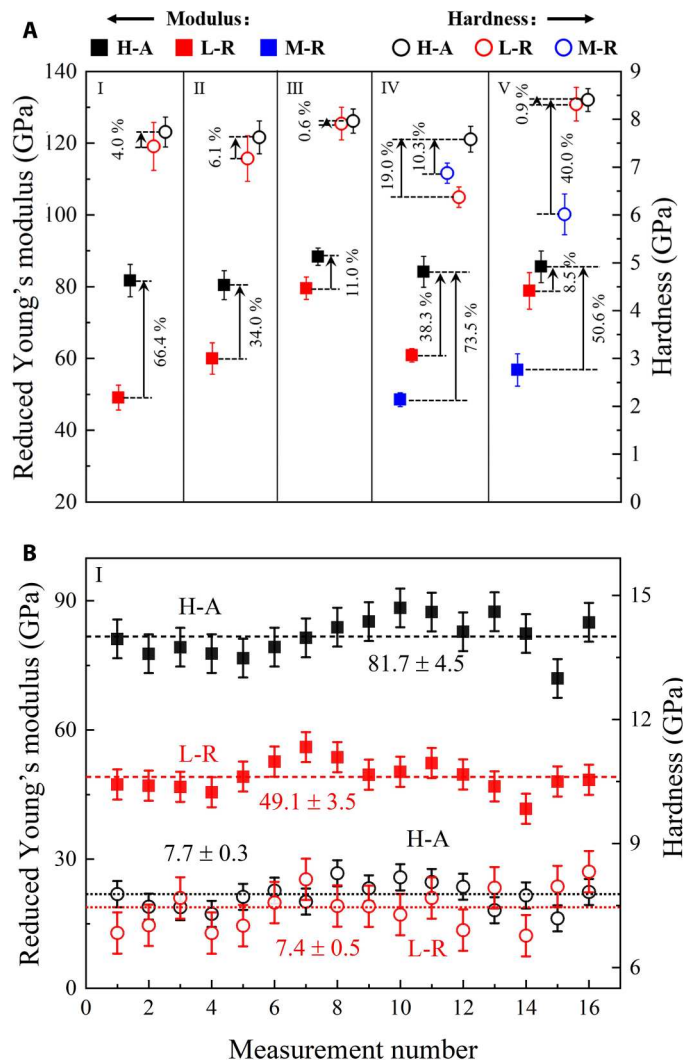
**Fig. 3. Comparison of the reduced Young′s modulus and hardness between the H-A sample and the rejuvenated one(s) for the glassy particles.** (**A**) Relative changes of the reduced Young′s modulus and hardness between the H-A sample and the L-R one or and the M-R one. (**B**) The reduced Young′s moduli and hardness of the H-A and L-R samples for particle I obtained by 16 indents of nanoindentation tests, with their average values indicated by the dotted lines.

of 8.5% in sequence. The corresponding increments of $H$ are 4.0, 19.0, 6.1, 0.6, and 0.9%, respectively. As a higher elastic modulus is generally accompanied with a higher hardness in glasses (44, 45), various degrees of decouplings between $E_r$ and $H$ occur in these glassy particles, with the most notable decoupling in particle I. Moreover, the increments of $E_r$ between the M-R sample and the H-A sample are even larger for glassy particles IV and V, with the value of 73.5 and 50.6%, respectively. The corresponding increment of $H$ increases to 40.0% for glassy particle V and abnormally reduces to 10.3% for glassy particle IV, which further confirms the decoupling between $E_r$ and $H$. Thence, the geological time scales′ aging-induced modulus increment should be >66.4% in particle I, >34.0% in particle II, and >11.0% in particle III by a relatively limited evaluation and >73.5% in particle IV and >50.6% in particle V by a more complete evaluation. To the best of our knowledge, such aging-

induced huge modulus increments in lunar glassy particles I, IV, and V have been seldom reported before in other glasses. Figure 3B shows representatively the detailed data of $E_r$ and $H$ of the L-R and H-A samples for glassy particle I. To reduce the experimental error, at least 16 indents were made for each sample. For glassy particle I, both $E_r$ and $H$ of the L-R sample fluctuate in a moderate range, with average values of 49.1 ± 3.5 and 7.4 ± 0.5 GPa, respectively. In sharp contrast, $E_r$ of the H-A sample is substantially higher than that of the L-R one, with an average value of ~81.7 ± 4.5 GPa, while $H$ of the H-A sample is quite close to that of the L-R one (the two values overlap in their 1-sigma uncertainty), with an average value of ~7.7 ± 0.3 GPa. The detailed data of $E_r$ and $H$ of the rejuvenated and H-A samples for other glassy particles can be found in fig. S5. In other words, geological time scales′ aging results in relatively huge increments of $E_r$, while there are much weaker effects on $H$ in these lunar glassy particles.

The structure characteristics of the rejuvenated and H-A samples for all the glassy particles were examined by TEM. Figure 4 (A and B) shows the cross-sectional TEM images of the L-R sample and the H-A one for glassy particle I showing the most extraordinary aging effects. The entire cross sections for both samples display a uniform contrast, which is a common feature of the amorphous phase. The corresponding halo-like selected-area electron diffraction (SAD) patterns in the insets of Fig. 4, A and B, as well as the maze-like high-resolution TEM (HRTEM) patterns in Fig. 4 (D and E) confirm the interior glassy structures for both the L-R and H-A samples. The glassy structures of the rejuvenated and H-A samples for other glassy particles are also verified in figs. S6 to S9. It confirms that all the glassy particles have retained the glassy structure even after aging for millions to billions of years. However, it seems that some discrepancies may exist between the H-A sample and the rejuvenated one(s) for these glassy particles. Generally, the contrast of the HRTEM image for the H-A sample is more homogeneous than that for the rejuvenated one(s), especially for glassy particle I with the H-A sample and the L-R one shown in Fig. 4 (E and D, respectively). Meanwhile, the comparison of the SAD pattern between the H-A sample and the L-R one shown in Fig. 4C indicates distinct structural changes in this lunar glassy particle after aging, as the diffractive halo radius of the H-A sample is obviously larger than that of the L-R one. Furthermore, we obtained the normalized one-dimensional static structure factor $S(q)$ ($q$ is the scattering vector) from the SAD patterns by using the profile analysis of SAD tools of the Digital Micrograph software, which is a powerful tool for studying the microstructure changes of the nanocrystalline and glassy materials (46, 47). The first maximum of $S(q)$ was fitted by a pseudo-Voigt function (48). The first peak position $q_1$ for glassy particle I shifted toward a higher value, with the mean value shift from 2.144 Å$^{-1}$ of the L-R sample to 2.246 Å$^{-1}$ of the H-A one, which indicates that the average interatomic distance is apparently decreased (note that the mean value of $q_1$ were obtained from three SAD patterns of three randomly selected regions in both the L-R and H-A samples). According to the power-law relationship in glass (49), $q_1 \cdot v_a^{\frac{1}{D_f}} = C$, where $v_a$ is the atomic volume, $D_f$ is the fractal dimension (ranging from 2.27 to 2.65 for silica glasses), and $C$ is a constant. Thence, $v_a$ of the H-A sample is about 0.884 to 0.900 times that of the L-R one. This result suggests that a sharp volume shrinkage between the H-A sample and the L-R one (10.0 to 11.6%) occurs in glassy particle I. Using the same analysis
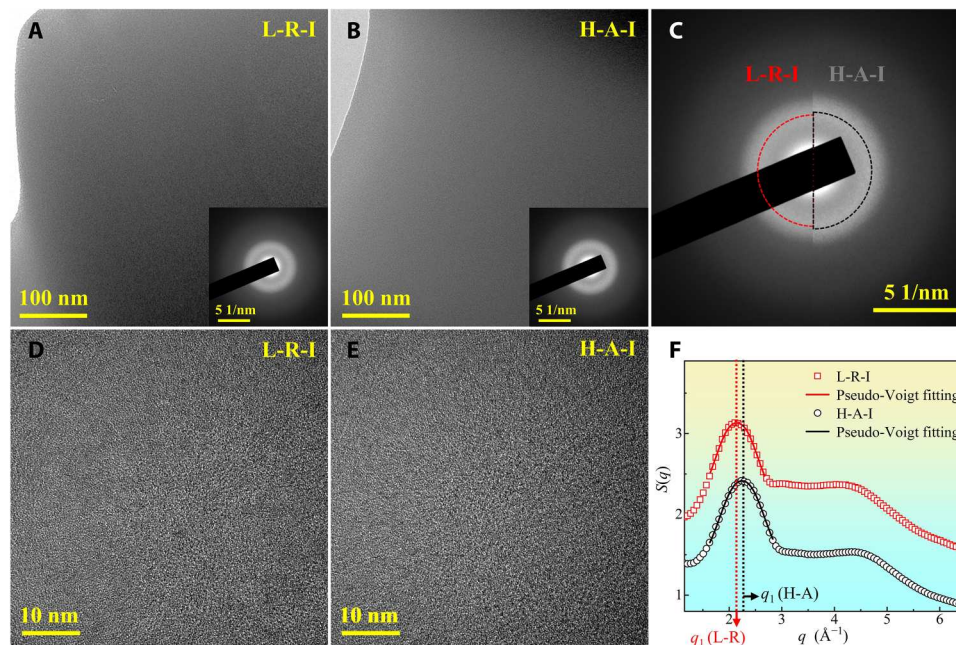
**Fig. 4. Structural characteristics of the L-R and H-A samples for glassy particle I.** Bright-field cross-sectional TEM images of (**A**) the L-R sample and (**B**) the H-A one. Each inset shows a diffractive halo-like SAD pattern, indicating the fully glassy structure. HRTEM images of (**D**) the L-R sample and (**E**) the H-A one. (**C**) Comparison of the SAD pattern between the L-R sample (left) and the H-A one (right). (**F**) Structure factor $S(q)$ of the L-R and H-A samples obtained from SAD patterns shown in (C).

method, volume shrinkages between the H-A sample and L-R one in glassy particles II, III, IV, and V are 5.3 to 6.2%, 2.0 to 2.4%, 5.5 to 6.4%, and 1.6 to 1.9%, respectively. Moreover, the volume shrinkages between the H-A sample and the M-R one in glassy particles IV and V are 10.8 to 12.5% and 7.3 to 8.4%, respectively. Therefore, the volume shrinkages after geological time scales' aging should be >10.0 to 11.6% in particle I, >5.3 to 6.2% in particle II, and >2.0 to 2.4% in particle III by a relatively limited evaluation using the slowly cooled sample and >10.8 to 12.5% in particle IV and >7.3 to 8.4% in particle V by a more complete evaluation using the fast cooled sample. To the best of our knowledge, in line with the corresponding huge modulus increments, such aging-induced huge volume reductions in lunar glassy particles I, IV, and V have either hardly been reported before in other glass systems.

Furthermore, to reveal the detailed structural discrepancy between the H-A sample and the rejuvenated one(s) for these glassy particles, we examine them by the high-angle annular dark field scanning TEM (HAADF-STEM) imaging and super EDS mapping. For glassy particle I with the nominal composition of $Si_{18.4}O_{59.8}Fe_{9.6}Ca_{4.1}Al_{3.6}Mg_{2.9}Ti_{1.0}Na_{0.6}$ (at %), a heterogeneous contrast, with nanoscale bright domains (~2 to 5 nm in diameter) randomly distributed in the dark matrix, can be observed in the L-R sample, as shown in Fig. 5A. According to the elemental maps and the EDS curves of the representative bright (#1) and dark (#2) areas shown in Fig. 5B, the bright domains are severely rich in Na; mildly rich in Mg; and mildly poor in Ca, O, and Si, relative to the dark matrix. In sharp contrast, a pretty homogeneous contrast is observed in the H-A sample, with all elements (i.e., Fe, O, Si, Al, Ti, Mg, Ca, and Na) homogeneously distributed, as shown in Fig. 5C. Meanwhile, few differences can be observed in the EDS curves between the selected areas #1 and #2 in Fig. 5C (Fig. 5D).

Similarly, the rejuvenated samples are generally more heterogeneous than the H-A ones for all other particles, according to the HAADF-STEM imagings and super EDS mappings of glassy particles II to V shown in figs. S10 to S13, respectively. Particularly, for glassy particle II with the nominal composition of $Si_{18.2}O_{58.8}Fe_{4.8}Ca_{4.5}Al_{5.7}Mg_{7.1}Ti_{0.4}K_{0.5}$ (at %), the bright domains in the L-R sample are mildly rich in Ca and K and mildly poor in Mg, Al, and Si, relative to the dark matrix, as shown in fig. S10. For glassy particle IV with the nominal composition of $Si_{24.6}O_{57.4}Fe_{3.1}Ca_{2.1}Al_{8.5}Mg_{2.6}Ti_{0.4}K_{1.3}$ (at %), the bright domains in the M-R sample are severely rich in Al; mildly rich in Ca, Mg, and Fe; and mildly poor in Si and K, relative to the dark matrix, as shown in fig. S12. For glassy particles III and V with the nominal composition of $Si_{18.0}O_{51.5}Fe_{8.6}Ca_{10.1}Al_{7.5}Mg_{2.0}Ti_{2.3}$ (at %) and $Si_{18.0}O_{56.2}Fe_{8.2}Ca_{4.8}Al_{5.8}Mg_{5.5}Ti_{1.5}$ (at %), respectively, no apparent element segregations happen in their rejuvenated samples as shown in figs. S11 and S13, indicating that the contrast heterogeneity in the HRTEM images for these samples shown in figs. S7 and S9 might be caused by the free volume (FV) segregations. The results above indicate that, in addition to the volume reduction, geological time scales' aging also leads to the homogenization of both element and FV distribution in these lunar glassy particles.

The structural heterogeneity of glass is associated with nanoscale structure fluctuation, which possibly inherits from spatially heterogeneous dynamics in supercooled liquids before glass transition (50). A higher cooling rate can reserve more structural characteristics of the melt in glass, which usually exhibits as a higher energy state with more structural defects, a higher friction temperature, and a lower density (51), as shown in Fig. 1. Generally, aging or structural relaxation lowers the energy state of glass by reducing its defect content, leading to a more densely packed and more
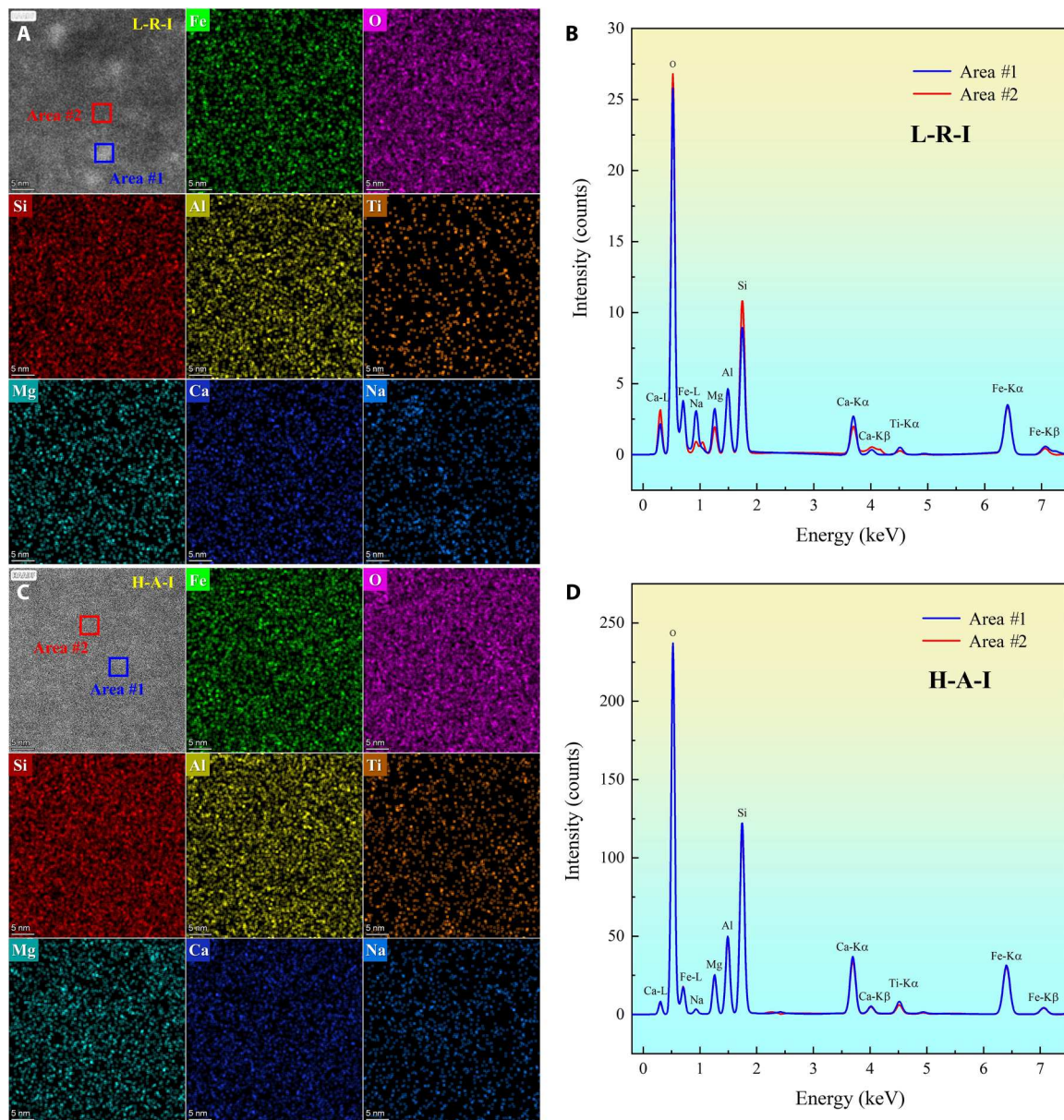
**Fig. 5. EDS analysis of the L-R and H-A samples for glassy particle I.** HAADF-STEM images and elemental maps of (**A**) the L-R sample and (**C**) the H-A one. EDS curves of the selected areas #1 and #2 in the HAADF-STEM images in (**B**) panel (A) and (**D**) panel (C).

homogeneous structure in the more relaxed (i.e., more stable) glass (*52*). Therefore, the rejuvenated sample with a higher cooling rate has a more loosely packed and more heterogeneous structure than the aged or relaxed one. For these lunar glassy particles (belongs to silicate glasses), the nanoscale heterogeneity in the rejuvenated samples should be inherited from their melts, of which the chemical heterogeneity is the intrinsic attribute (*53*), by heating them up to the supercooled liquid region and cooling them down. More preciously, the rejuvenated samples should have lower network connectivities with more segregated cations and FV and more nonbridging oxygens (NBOs) (*54*, *55*) and, hence, more loosely-packed structure than the H-A ones. Such structures might be dynamically favored and inherited from the supercooled liquids by

cooling (*56*). Upon aging or relaxation for an extremely long time, the "structural defects" (such as segregated cations, FV, and NBOs) in the lunar glasses are decreased by the atomic diffusion accompanied by bond breaking and building (*57*), leading to the more closely packed and more homogeneous stable lunar glasses.

The magnitude of the elastic moduli in glass is governed by both the atomic bond energy and the atomic packing density ($C_g$), of which the latter is more important (*58*). $C_g$ is defined as the ratio between the minimum theoretical volume occupied by the ions and the corresponding effective volume of glass, $C_g = \rho \sum f_i V_i / \sum f_i M_i$, for the *i*th constituent with $A_x B_y$ chemical formula, $V_i = 4/3\pi N(x r_A^3 + y r_B^3)$, where $\rho$ is the specific mass, $N$ is the Avogadro number, $r_A$ and $r_B$ are the ionic radii, $f_i$ is the molar fraction,

and $M_i$ is the molar mass (59). One the one hand, volume shrinkage will directly result in the increase of ρ and, hence, the increase of $C_g$. On the other hand, the homogenization of element distribution will also lead to the increase of $C_g$, as high values of $C_g$ are favored by chemical disorder (58). Therefore, the combined effect of both the volume shrinkage and the homogenization of element distribution led to the increments of $E$ in these lunar glassy particles after geological time scales' aging. As the increasing amplitude of $E$ was reported to be about four to six times that of ρ in other silicate glasses (45, 60, 61), the examined huge increments of $E$ in particles I, IV, and V (66.4, 73.5, and 50.6%, respectively) might be mainly caused by the corresponding volume shrinkages (10.0 to 11.6%, 10.8 to 12.5%, and 7.3 to 8.4% respectively). It is also supported by the result that a 70% reduction of $E$ was observed in the shear band (SB) region (62), where the reduction of ρ was less than 10% relative to the undeformed matrix in MGs (63, 64).

## DISCUSSION

### Decoupling mechanism between elastic modulus and hardness in the lunar glassy particles

The elastic modulus measures the material's resistance to elastic deformation, while hardness describes the material's ability to withstand surface indentation involving localized plastic deformation. Thence, the elastic modulus is only determined by the original structure, while hardness is determined by the instant structure during plastic deformation, which is also affected by the original one. To uncover the underlying decoupling mechanism between $E$ and $H$ in these lunar glassy particles, the load-displacement curves and the corresponding residual indent morphologies of the rejuvenated and H-A samples for these glassy particles were first examined.

As shown in Fig. 6A, except for glassy particle IV, apparent pop-ins indicated by the arrows, which correspond to the activation of SBs (65), can be observed in the representative load-displacement (P-h) curves for the other four glassy particles (the detailed nanoindentation curves of the H-A and rejuvenated samples for the five glassy particles can be found in figs. S14 and S15). Moreover, more pop-ins are observed in the P-h curves of the rejuvenated sample than in those of the H-A one for particles II, III, and V. It is in line with the residual indent morphologies shown in Fig. 6B that more SBs are observed in the rejuvenated sample than in that of the H-A one for particles II, III, and V. Note that, for particle I, more pop-ins exhibited in the P-h curve of the H-A sample than in that of the L-R one, which seems to contradict with the result that much more SBs are observed in the L-R sample than in the H-A one. It should be attributed to the reason that high-density shear banding deformation in the L-R sample of particle I suppresses the pop-ins (66). For particle IV, neither pop-ins show in the P-h curves nor apparent SBs show in the indents of the rejuvenated and H-A samples.

During indentation deformation, two competitive mechanisms, i.e., densification and shear flow, jointly determine the permanent deformation in glass (21). Generally, densification needs a lower activation stress, hence resulting in a lower hardness than shear flow (21). For the glassy particles I, II, III, and V, as more SBs formed in the rejuvenated sample than in the H-A one (Fig. 5), the proportion of shear flow in the rejuvenated sample might be larger than that in the H-A one and hence results in hardening effect in the

rejuvenated sample. That is why decoupling between the elastic modulus and hardness happens in these four particles. For another, the proportion of shear flow generally decreases as the network cation [$Si^{4+}$, $Al^{3+}$, and $B^{3+}$ (53)] content increases and the modifier cation [such as $Na^+$, $K^+$, $Ca^{2+}$, $Mg^{2+}$, and $Fe^{2+}$ (53)] content decreases in silicate glasses (21). Particle IV has relatively more network cations ($Si^{4+}$ and $Al^{3+}$ of ~33.1%) than other particles ($Si^{4+}$ and $Al^{3+}$ of ~22.0 to 25.5%) and hence might suppress the shear flow and shear banding deformation upon indentation. Its decoupling mechanism needs to be further clarified.

Furthermore, the microstructural evolution underneath the indenters of the rejuvenated and H-A samples for glassy particles I, IV, and V were elaborately examined. Note that the cross-sectional TEM specimens of the residual indents for these samples were fabricated by focused iron beam (FIB) in the positions indicated by the yellow rectangles shown in Fig. 6B.

For glassy particle I, plenty of SBs indicated by the arrows can be observed in the indent of the L-R sample as shown in Fig. 6B. It could be attributed to the more loosely packed structure with nanoscale heterogeneity and lower network connectivity of the L-R sample (Fig. 5, A and B), which is beneficial for the generation of multiple SBs (21, 67). Meanwhile, abundant nanocrystals formed underneath the indenter as shown in Fig. 7A, which should be ascribed to the greatly enhanced atomic mobility during shear deformation (68). Although single SB can be hardly distinguished, as all SBs interacted with each other, two main shear directions can still be roughly identified, which are indicated by the arrows in Fig. 7A. In the relatively more-compressed while less-sheared region (region a), the glassy structure almost remained inset with only some tiny nanocrystals according to the HRTEM image and the corresponding fast Fourier transform (FFT) image shown in Fig. 7B, while the structural heterogeneity of the glass in this region was greatly enhanced relative to the L-R sample shown in Fig. 4D, as plenty of big bright grains with diameters of dozens of nanometers and small dark particles with diameters of several nanometers formed. The HAADF-STEM image and super EDS results shown in fig. S16 (A and B) indicate that most elements were heterogeneously distributed in the remaining glass part (region a) of the indented L-R (I-L-R) sample for glassy particle I. Relative to the dark grains, the tiny bright particles (corresponding to the dark particles in Fig. 7B) are apparently rich in Na, Mg, Fe, Ca, and Ti while poor in O, Si, and Al. It indicates that severer elemental segregation happened in the less sheared regions in the L-R sample for glassy particle I upon indentation. Along the shear direction, the bright grains were refined with much more tiny dark particles, and nanocrystals formed in region b shown in Fig. 7C. Furthermore, in the severely sheared regions, plenty of nanocrystallines formed, such as monoclinic $Na_2Si_2O_5$ in region c (Fig. 7D), cubic $Fe_2O_3$ in region d (Fig. 7E), and tetragonal $SiO_2$ in region e (Fig. 7F). Moreover, high-density stacking faults (SFs) even formed in the $SiO_2$ crystalline in region f (Fig. 7G). Note that the less sheared region g has a structure similar to region a, as shown in Fig. 7H. Therefore, it can be seen that, when the L-R sample of glassy particle I was indented, its loosely packed structure with nanoscale heterogeneity and lower network connectivity facilitates the multiple shear banding deformation, which greatly improved the atomic mobility, hence resulting in, first, enhanced elemental segregation and, eventually, remarkable crystallization. In sharp contrast, no apparent SBs can be observed around or in the indent of the H-A sample for glassy
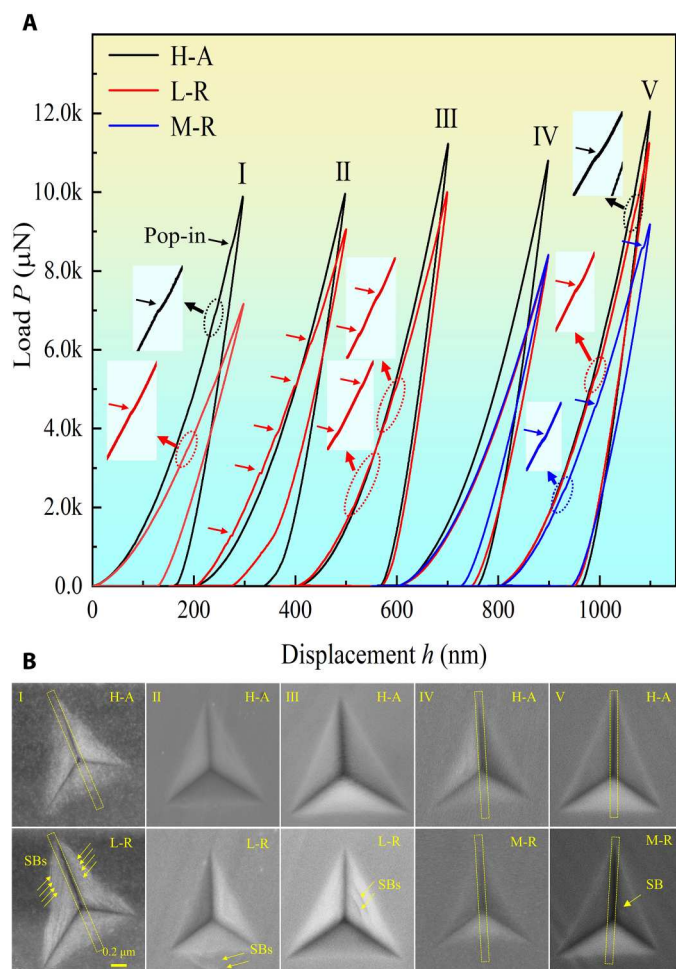
**Fig. 6. Deformation characteristics of the rejuvenated and H-A samples for the glassy particles I to V.** Representative load-displacement (*P-h*) curves (**A**) and residual indent morphologies (**B**) of the rejuvenated and H-A samples for glassy particles I to V.

particle I, as shown in Fig. 6B. In addition, no apparent SBs can be detected underneath the indenter, as shown in Fig. 7I. It should be attributed to the pretty homogeneous structure of this H-A sample (Fig. 5, C and D), which greatly inhibited the shear banding deformation (*67, 69*). The corresponding SAD pattern (inset in Fig. 7I) and HRTEM image (Fig. 7J) indicate that the H-A sample maintained a glassy structure after indentation tests for glassy particle I. Meanwhile, most elements were still homogeneously distributed in the indented H-A (I-H-A) sample (fig. S16C), and only slight differences can be observed between the representative bright area (#1) and dark area (#2; fig. S16D).

It has been well established that deformation-induced crystallization will results in both hardening and toughening effects in the glassy materials as the in situ formed crystals will effectively block the propagation of SBs, hence promoting multiple shear banding deformation (*70*). Moreover, deformation-induced twinning may also lead to hardening and toughening in the crystalline materials (*71*). Thence, the most notable decoupling phenomenon between elastic modulus and hardness in glassy particle I is attributed to the severe hardening effects of shear banding deformation–

induced crystallization and further twinning shown in Figs. 7 (A to H). In addition, the L-R sample should have much better plasticity than the H-A one for glassy particle I.

For glassy particle IV, neither apparent SBs nor crystals can be observed in all the M-R, L-R, and H-A samples after indentation, as shown in fig. S17. The representative SAD images [insets in fig. S17 (A to C)] and the corresponding HRTEM images (fig. S17, D to F) of the similar region underneath the indenter for the three samples confirm their glassy structures after indentation. Meanwhile, the HRTEM images of the three indented samples seem to maintain the similar structural heterogeneity compared to their corresponding unindented ones (fig. S8, E to G). Furthermore, to reveal a more detailed structural evolution for the three samples upon indentation, we compared their SAD patterns between the unindented sample and the indented one. Upon indentation, the first peak position $q_1$ shifted from 2.085 to 1.863 $\text{Å}^{-1}$, from 2.139 to 2.076 $\text{Å}^{-1}$, and from 2.193 to 2.191 $\text{Å}^{-1}$ for the M-R sample, the L-R one, and the H-A one, respectively, as shown in fig. S18. Hence, indentation-induced volume expansions are 29.1 to 34.8% and 7.0 to 8.2% in the M-R sample and the L-R one, respectively, while few volume expansions happened in the H-A sample upon indentation. It indicates that a higher proportion of shear flow (the mechanism accounts for volume expansion) happens in a more rejuvenated sample upon indentation for glassy particle IV. The largely enhanced proportion of shear flow in the M-R sample results in the abnormally enhanced hardness relative to the L-R one (Fig. 3A). Therefore, its decoupling mechanism between elastic modulus and hardness is identical to that of the other four particles, i.e., the hardening effect caused by the enhanced proportion of shear flow in the rejuvenated sample. However, without deformation-induced crystallization and twinning in the rejuvenated sample, its decoupling is weaker than that of glassy particle I. Note that the relatively abundant network cations do not really decrease the proportion of shear flow in the rejuvenated samples for glassy particle IV, probably because of their remarkable structural heterogeneity shown in fig. S12 (A to D), and some hidden SBs (*72*), which were reported recently in a bent heterogeneous MG and do not induce shear offsets in TEM images or pop-ins in *P-h* curves, may form in the rejuvenated samples for glassy particle IV (as well as for other particles).

For glassy particle V, an offset (indicated by the arrow), which should be caused by shear banding deformation, is observed in the M-R sample upon indentation, as shown in fig. S19A. However, no apparent SBs could be observed, which might be due to their very tiny size, as the indentation depth is relatively small. Meanwhile, no apparent SBs can be observed in the L-R and H-A samples after indentation, as shown in fig. S19 (B and C, respectively). No crystals formed in all the three samples, as the glassy structures of these samples are verified by the representative SAD images [insets in fig. S19 (A to C)] and the corresponding HRTEM images (fig. S19, D to F). Figure S20 reveals that the first peak position $q_1$ shifted from 2.155 to 2.187 $\text{Å}^{-1}$, from 2.212 to 2.148 $\text{Å}^{-1}$, and from 2.228 to 2.226 $\text{Å}^{-1}$ after indentation for the M-R sample, the L-R one, and the H-A one, respectively. Thence, a volume shrinkage of 3.3 to 3.9% and a volume expansion of 6.9 to 8.1% happen in the M-R sample and the L-R one, respectively. However, the structure of the H-A sample was almost unchanged upon indentation. It indicates that, relative to the H-A sample, a higher proportion of shear flow happens in the L-R one, while a
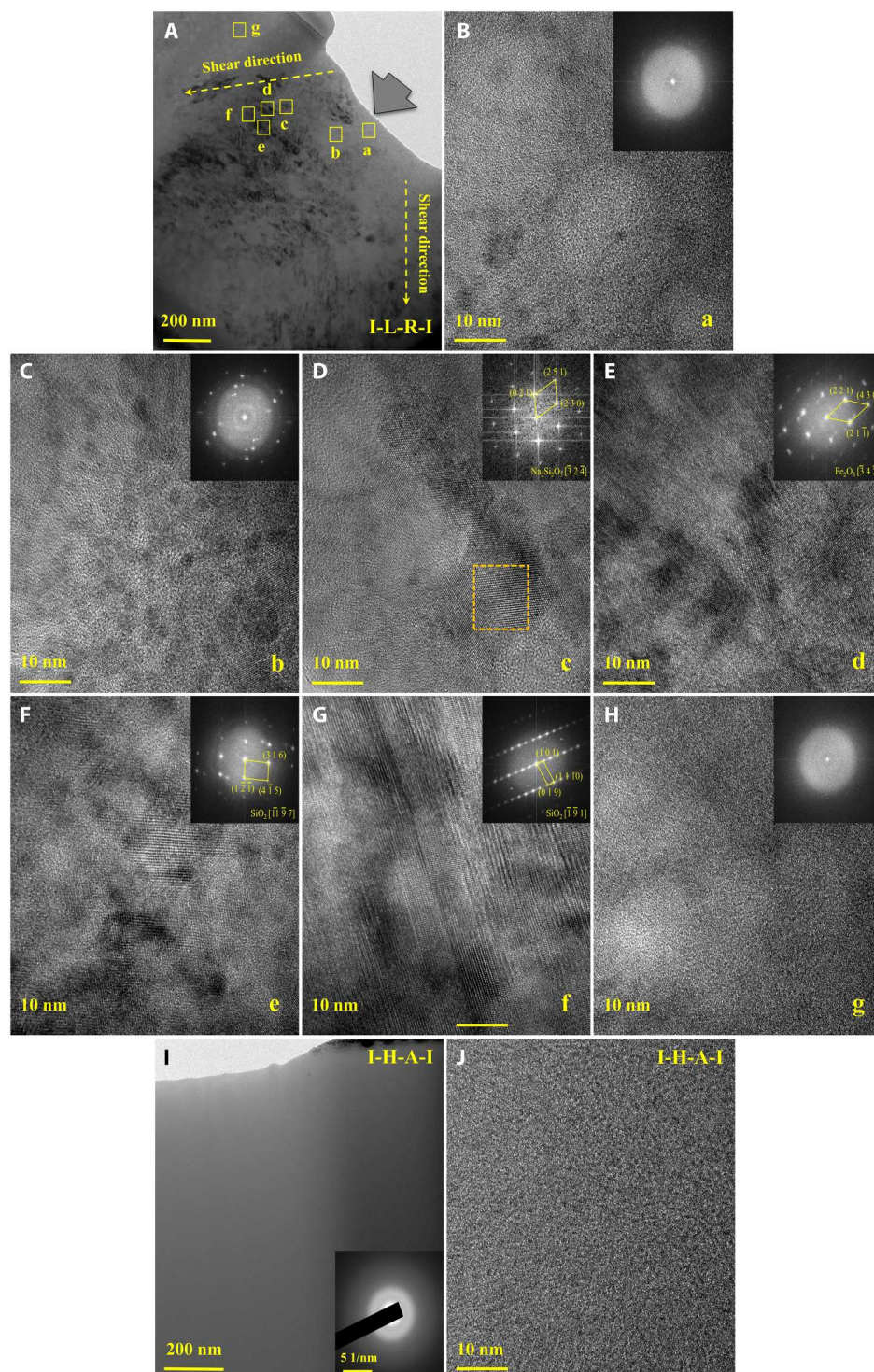
**Fig. 7. Cross-sectional structural characteristics of the I-L-R and I-H-A samples for glassy particle I.** Bright-field cross-sectional TEM micrograph of (**A**) the I-L-R sample and (**I**) the I-H-A one [the inset in (I) shows the corresponding SAD pattern]. HRTEM images of regions (**B**) a, (**C**) b, (**D**) c, (**E**) d, (**F**) e, (**G**) f, and (**H**) g of the sample in (A) [the insets in (B), (C), (E), (F), and (H) show the corresponding FFT images and the inset in (D) shows the FFT image corresponding to the rectangle area]. (**J**) HRTEM image of the sample in (I).

lower proportion of shear flow happens in the M-R one for glassy particle V. That is why a much weaker decoupling between the elastic modulus and hardness happens in such particle after a greater degree of rejuvenation (Fig. 3A).

## Dominant factors of aging effects in glasses

To clarify the dominant factors of aging effects in glasses, the available data of aging-induced changes of elastic modulus in various glasses are summarized in Fig. 8. More detailed data are supplied in table S2. It can be seen that the aging time scales are an important factor affecting the aging effects in glasses, as the aging-induced modulus change roughly increases as the time scales increase. Particularly, within a laboratorial time scale, aging can only lead to a mild modulus increment (mostly less than 10%) in all kinds of glasses, which were all annealed around or even beyond $T_g$ ($12$, $73$–$82$). In contrast, ultrastabilization, of which the effects were suggested to be equivalent to that of aging for hundreds to thousands of years according to the thermal evaluations, can lead to an obviously enhanced modulus increment as high as 19% in organic glass indomethacin (IMC) ($83$) and 22% in $Pd_{42.5}Ni_{42.5}P_{15}$ MG ($84$). For the lunar glasses in this study, the geological time scales' aging can result in a much greater modulus increment of above 66.4, 73.5, and 50.6% in glassy particles I, IV, and V, respectively. It may indicate that some so-called ultrastable glasses do not get the most stable state, and there is still plenty of room to stabilize further the glasses by prolonging aging time. However, it should be noted that there

will be a saturated value to the aging effect for a particular glass under a certain condition. By prolonging aging time, the glass approaches its lower limit of energy state (such as the ideal state) to exhibit the saturated aging effect. For instance, the ideal states have been achieved in some aged nanoscale polymer glasses [such as sphere ($26$) and thin film ($27$)], as their large free interfaces greatly accelerate the relaxation dynamics, leading to the fast approach to the ideally lowest limit of $T_f$ with a reduction of ~70 to 90 K relative to the values of their bulk samples. Such a huge $T_f$ reduction in standard aging in a bulk glass would require geological time scales ($27$). In this work, although the direct thermodynamic data regarding the energy state of the five lunar glassy particles (i.e., the H-A samples) are still missing, it is likely seen that a very low energy state (maybe already in a saturated state) has been achieved in these particles because they all have reached both structurally and chemically homogeneous states (Figs. 4E and 5, C and D, and figs. S6E, S10, C and D, S7E, S11, C and D, S8G, S12, E and F, S9G, and S13, E and F) after aging for geological time scales. It is also in line with the thermal results of the whole lunar glasses shown in Fig. 2B that the H-A sample have attained both more kinetic and thermodynamic stable state than the rejuvenated one.

The aging effects in glasses are apparently composition dependent in each time scale. Phenomenally, more complex systems will exhibit more notable aging effects as shown in Fig. 8. For instance, at a similar reduced temperature (annealing temperature divided by $T_g$), 1 hour and 900 hours of annealing can lead to 10 and 6% modulus increment in $Zr_{52.5}Cu_{17.9}Ni_{14.6}Al_{10}Ti_5$ MG ($74$) and $Zr_{46.75}Ti_{8.25}Cu_{7.5}Ni_{10}Be_{27.5}$ MG ($75$), respectively, while 17.7 years of annealing only leads to 4.3% modulus increment in $Ce_{70}Al_{10}Cu_{20}$ MG ($12$). The amber (with the chemical formula of $C_{10}H_{16}O$), which is aged for $1.1 \times 10^8$ years at $0.73T_g$, shows only 6.9% modulus increment ($7$). In sharp contrast, the lunar glassy particles I, IV, and V [with nominal composition of $Si_{18.4}O_{59.8}Fe_{9.6}Ca_{4.1}Al_{3.6}Mg_{2.9}Ti_{1.0}Na_{0.6}$, $Si_{24.6}O_{57.4}Fe_{3.1}Ca_{2.1}Al_{8.5}Mg_{2.6}Ti_{0.4}K_{1.3}$, and $Si_{18.0}O_{56.2}Fe_{8.2}Ca_{4.8}Al_{5.8}Mg_{5.5}Ti_{1.5}$ (at %), respectively] in this study exhibit more than 66.4, 73.5, and 50.6% modulus increment after aging below $0.41T_g$ for similar time scales. Note that, although the lunar glassy particles II and III show only 34 and 11% modulus increments, respectively, by the very limited evaluation, they may also exhibit more notable modulus increments (probably above 50%) by a more complete evaluation, as the lunar glassy particles IV and V exhibit similar modulus increments (38.3 and 8.5%) with particles II and III, respectively, by the same limited evaluation and show much enhanced modulus increments (73.5 and 50.6%, respectively) by a more complete evaluation. Therefore, the extraordinary aging effects of a huge modulus increment should be the common feature for these lunar glasses. It should be due to the reason that the complex multicomponent of the lunar glasses, which were naturally chosen by impacting the lunar regolith on the moon, can enlarge their configuration space and hence enlarge their aging space ($85$). These five lunar glassy particles display different aging effects (maybe already reach the saturated values), mainly because of their different compositions. Hence, for a given glass, as aging time increases, the aging effect increases toward a saturated value, which is mainly determined by the composition.

Previously, ultrastabilization was achieved by controlling the deposition condition ($25$, $83$). Later, it was demonstrated that ultrastabilization could be achieved by glass-glass transition in the
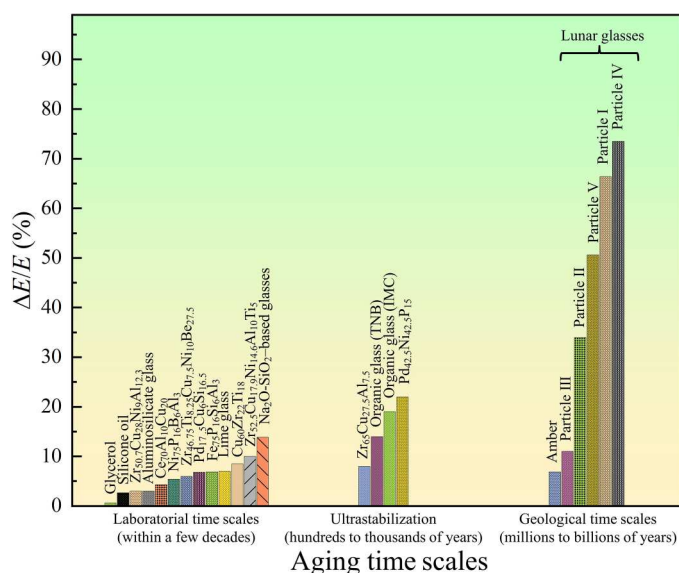


**Fig. 8. The changes of Young's modulus in various glasses by different time scales' aging ($\Delta E/E$ is the proportion of Young's modulus change).** The modulus data from the studies on glycerol ($76$), silicone oil ($77$), $Zr_{50.7}Cu_{28}Ni_9Al_{12.3}$ ($73$), aluminosilicate glass ($82$), $Ce_{70}Al_{10}Cu_{20}$ ($12$), $Ni_{75}P_{16}B_6Al_3$ ($78$), $Zr_{46.75}Ti_{8.25}Cu_{7.5}$ $Ni_{10}Be_{27.5}$ ($75$), $Pd_{17.5}Cu_6Si_{16.5}$ ($78$), $Fe_{75}P_{16}Si_6Al_3$ ($78$), lime glass ($80$), $Cu_{60}Zr_{22}Ti_{18}$ ($79$), $Zr_{52.5}Cu_{17.9}Ni_{14.6}Al_{10}Ti_5$ ($74$), $Na_2O$-$SiO_2$–based glasses ($81$), $Zr_{65}Cu_{27.5}Al_{7.5}$ ($25$), organic glass [TNB (trisnaphthylbenzene)] ($83$), organic glass (IMC) ($83$), $Pd_{42.5}$ $Ni_{42.5}P_{15}$ ($84$), and amber ($7$). Note that the ultrastabilization-induced modulus changes were regarded as equal to those induced by aging for hundreds to thousands of years. This is because the energy states of the man-made ultrastable glasses are equivalent to those resulting from natural aging over hundreds to thousands of years, as determined by thermal evaluations ($25$, $83$, $84$).

$Pd_{42.5}Ni_{42.5}P_{15}$ MG, leading to a greater modulus increment than others (*84*). Recently, HE designing was suggested to facilitate glass-glass transition in MGs, which also resulted in a much enhanced modulus increment of 9.6% in NbNiZrTiCo, 12.5% in NbNiZrTiCuCo, and 31% in NbNiZrTiCu HE MG (HEMG) (*85*). Therefore, HE might be beneficial to enlarge the aging effects in glasses, as its sluggish diffusion effect will dynamically elevate the quenched glass to a high energy state (*85*) and maintain more intrinsic structural heterogeneities, which will reversely enlarge the aging space. Because the configurational entropy of these lunar glasses is as high as $1.30R$ to $1.57R$ ($R$ is the gas constant), HE might be another factor for their extraordinary aging effects.

Furthermore, there are various minor elements, such as Ca, Al, Mg, Ti, Na, or K (note that, apart from Si and O, the other elements can all be regarded as minor elements for their relatively low content from the perspective of material science), which may also play a crucial role in determining their huge aging effects in these lunar glasses. For instance, Ca, Mg, and Na; Ca, Mg, and K; and Ca, Mg, Al, and K might be the crucial minor elements in glassy particles I, II, and IV, respectively, according to the EDS results shown in Fig. 4 and figs. S6 and S8. Meanwhile, in these lunar glassy particles, it seems that the particles with a small amount of alkali metal (i.e., particle I with Na and particles II and IV with K) show more notable aging effects than the other particles (i.e., particles III and V). It might be attributed to the mixed alkali-alkaline earth effect (*86*), which can promote the diffusion of the related ions, especially for those with smaller size. That might be why glassy particle I shows the most notable aging effects among these lunar glassy particles. In addition, as the elemental separation happens in a specific composition range for the alkali silicate melts (*87*), the most notable aging effects of glassy particle I, which were at least caused partially by the obvious elemental separation in its rejuvenated sample, might be also determined by its special composition. The aging-induced homogenization of the minor elements may promote the lunar glass to approach a more stable state by forming a higher atomic packing density, hence leading to a larger modulus increment (*58*). As the compositions of these lunar glasses are very complex, more definite conclusions requires precise control of the sample composition. This will be carried out by the developing simulated lunar glasses in our further work. Regardless, the energy state and properties of glass can be controlled effectively by adding proper minor elements.

In summary, the extraordinary aging effects were revealed in five representative lunar glassy particles, which were selected from the lunar regolith returned by Chang'e-5 mission, via TEM observation and nanoindentation tests. It is demonstrated that the H-A samples, which have experienced geological time scales' aging, have substantially higher Young's modulus (with an increment of more than dozens of percentages) but have more comparable hardness relative to that of the rejuvenated ones for these glassy particles. In other words, varied degrees of decoupling between modulus and hardness happen in these glassy particles. The huge modulus increments in these samples are attributed to both the sharp volume shrinkage and the homogenization of elemental distribution, with the former being the dominant factor. The relatively comparable hardness between the H-A sample and the rejuvenated ones is due to their different deformation mode. Generally, a higher proportion of shear flow happens in the rejuvenated samples than that in the H-A one, leading to more SBs in the former than in the later and hence results in different degrees of hardening effect in the rejuvenated

samples for these glassy particles. Particularly, for glassy particle I showing the most notable decoupling phenomenon, the deformation-induced crystallization and further nanotwinning, which was caused by multiple shear banding deformation, lead to substantial hardening in the L-R sample with obvious heterogeneous structure, while much fewer SBs formed in the H-A sample with a pretty homogeneous structure. By comparing the aging effects over different time scales in various glasses, the extraordinary aging effects in these lunar glasses should be mainly attributed to the natural selected complex compositions and intrinsic structures (in line with the criterion of HE and minor element doping that can greatly enhance the energy state and structural heterogeneity of the quenched glass and hence enlarge the aging space of glass) under the special lunar conditions and the extensive aging time. HE designing via multicomponent mixing and doping of proper minor elements may enlarge the aging space and hence facilitate enlarging aging effects and extending the range of glassy properties. The discovery of such extraordinary aging effects in the lunar glasses holds potential benefits for developing high-performance and stable glassy materials for radiation protection and space explorations.

## MATERIALS AND METHODS

The lunar regolith samples used in this study were scooped from the lunar surface in Chang'e-5 lunar exploration program. The sampling site is located in the northeastern Oceanus Procellarum with longitude and latitude of 51.916°W and 43.058°N. The lunar regolith sample numbered CE5C0400 was applied from the China National Space Administration. To examine the thermal properties of the lunar glasses, a spoon of lunar regolith samples of ~20 mg were characterized by a differential scanning calorimeter (DSC; NETZSCH 404 F3) at a heating rate of 40 K/min in high-purity argon atmosphere. As shown in Fig. 2A, $T_g$ and $T_x$ of lunar glasses were 936 and 1030 K, respectively, which provides a basis for our subsequent rejuvenation treatment. Moreover, to study the aging effect on the thermal properties of the lunar glasses, a new spoon of lunar regolith sample (~20 mg) was first erased in the thermal history (i.e., heated to 973 K in the supercooled liquid region at 40 K/min, held for 60 s, and then cooled down to RT at 40 K/min under a purified argon atmosphere in the DSC chamber) and then characterized by a DSC at a heating rate of 40 K/min. Five typical returned (i.e., H-A) glassy particles (four spherules with diameters ranging from 20 to 53 μm and one ellipsoid of similar size), termed as particles I to V, as shown in fig. S2 (A to E), were selected through morphologic observation using field-emission scanning electron microscopy (ZEISS Gemini300). The rejuvenated samples for these glassy particles were obtained by heating them up to the supercooled liquid region of 973 K, holding for 60 s, and then cooling down to RT at controlled cooling rates. Such rejuvenation treatment has been frequently applied in many glasses (*88, 89*). A slower cooling rate of ~40 K/min was applied for all the glassy particle, by which the sample is termed as the L-R one. Moreover, a faster cooling rate of ~240 K/s was applied for glassy particles IV and V, by which the sample is termed as the M-R one. Note that, to eliminate the influence of $O_2$, $H_2O$, and other corrosive medium, the L-R samples were obtained in the DSC (NETZSCH 404 F3) under the protection of a purified argon atmosphere, and the M-R samples were obtained in the homemade

thermal treatment device (shown in fig. S21) with a vacuum degree of $10^{-4}$ Pa.

The microstructures of the selected particles were examined using TEM (JEM-F200) and aberration-corrected TEM (Thermo Fisher Scientific Spectra 300) equipped with a high-brightness field-emission gun (X-FEG), double Cs corrector from CEOS, and a fast-speed Super-X EDS detector. The cross-sectional TEM samples were prepared using a dual FIB system (Ethos NX 5000). RT nanoindentation tests of glassy particle samples were conducted in a Nanoindenter (Bruker Hysitron, TI 980) equipped with a Berkovich indenter. Before indentation, prisms with adequate sizes, as shown in fig. S2 (F to J), were cut from the particles and fixed on copper meshes via FIB. Then, the upper surface of each prism was carefully polished to a smooth plane by FIB using gradually reduced current. The constant strain rate model with strain rate of 0.05 s$^{-1}$ was applied. The maximum penetration depth was set as 300 nm, which was far below 10% of the sample thickness for the purpose of avoiding substrate effect. Before tests, the tip of the indenter was carefully calibrated on standard fused silica. The hardness and reduced Young's modulus were extracted from load-displacement curves via the Oliver-Pharr method (90). An allowable drift rate of 0.005 nm s$^{-1}$ was provided to set the thermal stability criterion for initiating the test, which is 10-fold smaller than the default value generally used in tests. For glassy particle I, at least 16 indents were made for each sample. For other particles with relatively small sizes, at least 10 indents were made for each sample. The residual indents were imaged by scanning electron microscopy (Gemini300). Moreover, the cross-sectional TEM specimens of the residual indents for rejuvenated and H-A samples for glassy particles I, IV, and V were elaborately fabricated by FIB.

## Supplementary Materials

**This PDF file includes:**
Figs. S1 to S21
Tables S1 and S2
References

## REFERENCES AND NOTES

1. G. S. Parks, H. M. Huffman, Glass as a fourth state of matter. *Science* **64**, 363–364 (1926).
2. T. Vogt, T. Shinbrot, Editorial: Overlooking glass? *Phys. Rev. Applied.* **3**, 050001 (2015).
3. J. C. Mauro, Decoding the glass genome. *Curr. Opin. Solid State Mater. Sci.* **22**, 58–64 (2018).
4. W. H. Wang, Dynamic relaxations and relaxation-property relationships in metallic glasses. *Prog. Mater. Sci.* **106**, 100561 (2019).
5. E. D. Zanotto, Do cathedral glasses flow? *Am. J. Phys.* **66**, 392–395 (1998).
6. O. Gulbiten, J. C. Mauro, X. Guo, O. N. Boratav, Viscous flow of medieval cathedral glass. *J. Am. Ceram. Soc.* **101**, 5–11 (2017).
7. T. Pérez-Castañeda, R. J. Jimenez-Rioboo, M. A. Ramos, Two-level systems and boson peak remain stable in 110-million-year-old amber glass. *Phys. Rev. Lett.* **112**, 165901 (2014).
8. R. C. Welch, J. R. Smith, M. Potuzak, X. J. Guo, B. F. Bowden, T. J. Kiczenski, D. C. Allan, E. A. King, A. J. Ellison, J. C. Mauro, Dynamics of glass relaxation at room temperature. *Phys. Rev. Lett.* **110**, 265901 (2013).
9. S. F. Swallen, K. L. Kearns, M. K. Mapes, Y. S. Kim, R. J. McMahon, M. D. Ediger, T. Wu, L. Yu, S. Satija, Organic glasses with exceptional thermodynamic and kinetic stability. *Science* **315**, 353–356 (2007).
10. Y. L. Guo, A. Morozov, D. Schneider, J. W. Chung, C. Zhang, M. Waldmann, N. Yao, G. Fytas, C. B. Arnold, R. D. Priestley, Ultrastable nanostructured polymer glasses. *Nat. Mater.* **11**, 337–343 (2012).
11. P. Luo, C. R. Cao, F. Zhu, Y. M. Lv, Y. H. Liu, P. Wen, H. Y. Bai, G. Vaughan, M. Di Michiel, B. Ruta, W. H. Wang, Ultrastable metallic glasses formed on cold substrates. *Nat. Commun.* **9**, 1389 (2018).
12. Y. Zhao, B. S. Shang, B. Zhang, X. Tong, H. B. Ke, H. Y. Bai, W. H. Wang, Ultrastable metallic glass by room temperature aging. *Sci. Adv.* **8**, eabn3623 (2022).
13. N. E. B. Zellner, Lunar impact glasses: Probing the moon's surface and constraining its impact history. *J. Geophys. Res. Planets* **124**, 2686–2702 (2019).
14. T. Long, Y. Q. Qian, M. D. Norman, K. Miljkovic, C. Crow, J. W. Head, X. C. Che, R. Tartèse, N. Zellner, X. F. Yu, S. W. Xie, M. Whitehouse, K. H. Joy, C. R. Neal, J. F. Snape, G. S. Zhou, S. J. Liu, C. Yang, Z. Q. Yang, C. Wang, L. Xiao, D. Y. Liu, A. Nemchin, Constraining the formation and transport of lunar impact glasses using the ages and chemical compositions of Chang'e-5 glass beads. *Sci. Adv.* **8**, eabq2542 (2022).
15. M. D. Norman, F. Jourdan, S. S. M. Hui, Impact history and regolith evolution on the moon: Geochemistry and ages of glasses from the Apollo 16 site. *J. Geophys. Res. Planets* **124**, 3167–3180 (2019).
16. L. P. Keller, D. S. McKay, The nature and origin of rims on lunar soil grains. *Geochim. Cosmochim. Acta* **61**, 2331–2341 (1997).
17. C. L. Li, H. Hu, M. F. Yang, Z.-Y. Pei, Q. Zhou, X. Ren, B. Liu, D. W. Liu, X. G. Zeng, G. L. Zhang, H. B. Zhang, J. J. Liu, Q. Wang, X. J. Deng, C. J. Xiao, Y. G. Yao, D. S. Xue, W. Zuo, Y. Su, W. B. Wen, Z. Y. Ouyang, Characteristics of the lunar samples returned by Chang'E-5 mission. *Natl. Sci. Rev.* **9**, nwab188 (2022).
18. S. Boble, The lunar regolith, in *Proceeding of the Lunar Regolith Simulant Workshop* (Lunar and Planetary Institute, 2009).
19. Y. Wang, K. Zhang, Y. H. Feng, Y. S. Li, W. Q. Tang, Y. T. Zhang, B. C. Wei, Z. Hu, Excellent irradiation tolerance and mechanical behaviors in high-entropy metallic glasses. *J. Nucl. Mater.* **527**, 151785 (2019).
20. K. M. Cannon, J. F. Mustard, S. W. Parman, E. C. Sklute, M. D. Dyar, R. F. Cooper, Spectral properties of Martian and other planetary glasses and their detection in remotely sensed data. *J. Geophys. Res. Planets* **122**, 249–268 (2017).
21. T. Rouxel, J.-I. Jang, U. Ramamurty, Indentation of glasses. *Prog. Mater. Sci.* **121**, 100834 (2021).
22. D. P. Birnie III, M. D. Dyar, Cooling rate calculations for silicate glasses. *J. Geophys. Res.* **16**, 509–513 (1986).
23. C. Y. Fang, H. Yinnon, D. R. Uhlmann, Cooling rates for glass containing lunar compositions. *J. Geophys. Res.* **88**, A907–A911 (1983).
24. H. Zhang, X. Zhang, G. Zhang, K. Q. Dong, X. J. Deng, X. S. Gao, Y. D. Yang, Y. Xiao, X. Bai, K. X. Liang, Y. W. Liu, W. B. Ma, S. F. Zhao, C. Zhang, X. J. Zhang, J. Song, W. Yao, H. Chen, W. H. Wang, Z. G. Zou, M. F. Yang, Size, morphology, and composition of lunar samples returned by Chang'E-5 mission. *Sci. China Phys. Mech. Astron.* **65**, 229511 (2021).
25. H. B. Yu, Y. S. Luo, K. Samwer, Ultrastable metallic glass. *Adv. Mater.* **25**, 5904–5908 (2013).
26. X. Monnier, J. Colmenero, M. Wolf, D. Cangialosi, Reaching the ideal glass in polymer spheres: Thermodynamics and vibrational density of states. *Phys. Rev. Lett.* **126**, 118004 (2021).
27. V. M. Boucher, D. Cangialosi, A. Alegria, J. Colmenero, Reaching the ideal glass transition by aging polymer films. *Phys. Chem. Chem. Phys.* **19**, 961–965 (2017).
28. J. W. Delano, Pristine lunar glasses: Criteria, data, and implications. *J. Geophys. Res. Solid Earth* **91**, 201–213 (1986).
29. R. A. Zeigler, R. L. Korotev, B. L. Jolliff, L. A. Haskin, C. Floss, The geochemistry and provenance of Apollo 16 mafic glasses. *Geochim. Cosmochim. Acta* **70**, 6050–6067 (2006).
30. G. H. Heiken, D. T. Vaniman, B. M. French, *Lunar Sourcebook, A User's Guide to the Moon.* (Cambridge Univ. Press, 1991).
31. S. V. Ketov, Y. H. Sun, S. Nachum, Z. Lu, A. Checchi, A. R. Beraldin, H. Y. Bai, W. H. Wang, D. V. Louzguine-Luzgin, M. A. Carpenter, A. L. Greer, Rejuvenation of metallic glasses by non-affine thermal strain. *Nature* **524**, 200–203 (2015).
32. R. Zhao, L. Q. Shen, D. D. Xiao, C. Chang, Y. Huang, J. H. Yu, H. P. Zhang, M. Liu, S. F. Zhao, W. Yao, Z. Lu, B. A. Sun, H. Y. Bai, Z. G. Zou, M. F. Yang, W. H. Wang, Diverse glasses revealed from Chang'E-5 lunar regolith. *Natl. Sci. Rev.* **nwad079**, 10.1093/nsr/nwad079, (2023).
33. R. O. Pepin, J. A. Eddy, R. B. Merrill, The ancient sun: Fossil record in the earth, moon and meteorites, in *Proceedings of the Conference, Boulder, CO* (OSTI, 1979).
34. S. K. Noble, L. P. Keller, C. M. Pieters, Evidence of space weathering in regolith breccias I: Lunar regolith breccias. *Meteorit. Planet. Sci.* **40**, 397–408 (2005).
35. N. Ollier, S. Girard, S. Peuget, Radiation effects in glass, in *Encyclopedia of Glass Science, Technology, History, and Culture* (Wiley, 2021), pp. 405–414.
36. K. Sun, G. Wang, Y. W. Wang, H. C. Chen, L. Yan, S. Pauly, Y. H. Wu, H. Weber, Q. Wang, B. Huang, Y. D. Jia, J. Yi, Q. J. Zhai, Structural rejuvenation and relaxation of a metallic glass induced by ion irradiation. *Scr. Mater.* **180**, 34–39 (2020).
37. L. Huang, Z. Q. Chen, P. Huang, X. K. Meng, F. Wang, Irradiation-induced homogeneous plasticity in amorphous/amorphous nanolaminates. *J. Mater. Sci. Technol.* **57**, 70–77 (2020).
38. L. T. Chen, X. T. Ren, Y. N. Mao, J. J. Mao, X. Y. Zhang, T. T. Wang, M. L. Sun, T. S. Wang, M. M. Smedskjaer, H. B. Peng, Radiation effects on structure and mechanical properties of borosilicate glasses. *J. Nucl. Mater.* **552**, 153025 (2021).

39. Y. Langevin, J. R. Arnold, The evolution of the lunar regolith. *Annu. Rev. Earth Planet. Sci.* **5**, 449–489 (1977).

40. P. Q. Nguyen, N. E. B. Zellner, Using size and composition to assess the quality of lunar impact glass ages. *Geosciences* **9**, 85 (2019).

41. L. P. Keller, E. L. Berger, S. L. Zhang, R. Christoffersen, Solar energetic particle tracks in lunar samples: A transmission electron microscope calibration and implications for lunar space weathering. *Meteorit. Planet. Sci.* **56**, 1685–1707 (2021).

42. Q.-L. Li, Q. Zhou, Y. Liu, Z. Y. Xiao, Y. T. Lin, J.-H. Li, H.-X. Ma, G.-Q. Tang, S. Guo, X. Tang, J.-Y. Yuan, J. Li, F.-Y. Wu, Z. Y. Ouyang, C. L. Li, X.-H. Li, Two-billion-year-old volcanism on the moon from Chang'e-5 basalts. *Nature* **600**, 54–58 (2021).

43. X. C. Che, A. Nemchin, D. Y. Liu, T. Long, C. Wang, M. D. Norman, K. H. Joy, R. Tartese, J. Head, B. Jolliff, J. F. Snape, C. R. Neal, M. J. Whitehouse, C. Crow, G. Benedix, F. Jourdan, Z. Q. Yang, C. Yang, J. H. Liu, S. W. Xie, Z. M. Bao, R. L. Fan, D. P. Li, Z. S. Li, S. G. Webb, Age and composition of young basalts on the moon, measured from samples returned by Chang'e-5. *Science* **374**, 887–890 (2021).

44. P. Vullo, M. J. Davis, Comparative study of micro-indentation and Chevron notch fracture toughness measurements of silicate and phosphate glasses. *J. Non Cryst. Solids* **349**, 180–184 (2004).

45. S. Striepe, M. M. Smedskjaer, J. Deubener, U. Bauer, H. Behrens, M. Potuzak, R. E. Youngman, J. C. Mauro, Y. Z. Yue, Elastic and micromechanical properties of isostatically compressed soda–lime–borate glasses. *J. Non Cryst. Solids* **364**, 44–52 (2013).

46. G. Wu, X. Zheng, P. Cui, H. Jiang, X. Wang, Y. Qu, W. Chen, Y. Lin, H. Li, X. Han, Y. Hu, P. Liu, Q. Zhang, J. Ge, Y. Yao, R. Sun, Y. E. Wu, L. Gu, X. Hong, Y. Li, A general synthesis approach for amorphous noble metal nanosheets. *Nat. Commun.* **10**, 4855 (2019).

47. C. Gammer, C. Mangler, C. Rentenberger, H. P. Karnthaler, Quantitative local profile analysis of nanomaterials by electron diffraction. *Scr. Mater.* **63**, 312–315 (2010).

48. F. Spieckermann, D. Şopu, V. Soprunyuk, M. B. Kerber, J. Bednarčík, A. Schökel, A. Rezvan, S. Ketov, B. Sarac, E. Schafler, J. Eckert, Structure-dynamics relationships in cryogenically deformed bulk metallic glass. *Nat. Commun.* **13**, 127 (2022).

49. D. Ma, A. D. Stoica, X. L. Wang, Power-law scaling and fractal nature of medium-range order in metallic glasses. *Nat. Mater.* **8**, 30–34 (2009).

50. M. D. Ediger, Spatially heterogeneous dynamics in supercooled liquids. *Annu. Rev. Phys. Chem.* **51**, 99–128 (2000).

51. C. Levelut, R. Le Parc, A. Faivre, B. Champagnon, Influence of thermal history on the structure and properties of silicate glasses. *J. Non Cryst. Solids* **352**, 4495–4499 (2006).

52. S. Nemilov, Physical ageing of silicate glasses. *Glass Sci. Technol.* **76**, 33–42 (2003).

53. G. S. Henderson, G. Calas, J. F. Stebbins, The structure of silicate glasses and melts. *Elements* **2**, 269–273 (2006).

54. S. Locker, J. A. Clark, S. K. Sundaram, Structural modifications of soda-lime silicate glasses using femtosecond pulse-laser irradiation. *Int. J. Appl. Glass Sci.* **12**, 25–35 (2020).

55. A. Rahman, G. Mariotto, E. Cattaruzza, E. Trave, F. Gonella, A. Quaranta, Thermal annealing and laser induced structural rearrangement and silver state modification in Ag$^+$-Na$^+$ ion-exchanged silicate glasses studied by Raman spectroscopy. *J. Non Cryst. Solids* **552**, 120455 (2021).

56. D. R. Neuville, C. Le Losq, Link between medium and long-range order and macroscopic properties of silicate glasses and melts. *Rev. Mineral. Geochem.* **87**, 105–162 (2022).

57. D. B. Dingwell, S. L. Webb, Relaxation in silicate melts. *Eur. J. Mineral.* **2**, 427–449 (1990).

58. T. Rouxel, Elastic properties and short-to medium-range order in glasses. *J. Am. Ceram. Soc.* **90**, 3019–3039 (2007).

59. D. R. Lide, *Handbook of Chemistry and Physics* (CRC Press, Taylor & Francis, ed. 86, 2005).

60. S. Spinner, A. Napolitano, Relation between refractive index and elastic moduli of a borosilicate glass after heat-treatment. *J. Am. Ceram. Soc.* **39**, 390–394 (1956).

61. K. G. Aakermann, K. Januchta, J. A. L. Pedersen, M. N. Svenson, S. J. Rzoska, M. Bockowski, J. C. Mauro, M. Guerette, L. P. Huang, M. M. Smedskjaer, Indentation deformation mechanism of isostatically compressed mixed alkali aluminosilicate glasses. *J. Non Cryst. Solids* **426**, 175–183 (2015).

62. S. V. Ketov, H. K. Nguyen, A. S. Trifonov, K. Nakajima, D. V. Louzguine-Luzgin, Huge reduction of Young's modulus near a shear band in metallic glass. *J. Alloys Compd.* **687**, 221–226 (2016).

63. V. Schmidt, H. Rösner, M. Peterlechner, G. Wilde, P. M. Voyles, Quantitative measurement of density in a shear band of metallic glass monitored along its propagation direction. *Phys. Rev. Lett.* **115**, 035501 (2015).

64. H. Rosner, M. Peterlechner, C. Kubel, V. Schmidt, G. Wilde, Density changes in shear bands of a metallic glass determined by correlative analytical transmission electron microscopy. *Ultramicroscopy* **142**, 1–9 (2014).

65. C. A. Schuh, T. G. Nieh, A nanoindentation study of serrated flow in bulk metallic glasses. *Acta Mater.* **51**, 87–99 (2003).

66. H. Huang, M. Q. Jiang, J. W. Yan, New evidences for understanding the serrated flow and shear band behavior in nanoindentation of metallic glasses. *J. Alloys Compd.* **857**, 157587 (2021).

67. A. L. Greer, Y. Q. Cheng, E. Ma, Shear bands in metallic glasses. *Mater. Sci. Eng.* **74**, 71–132 (2013).

68. J. J. Kim, Y. Choi, S. Suresh, A. S. Argon, Nanocrystallization during nanoindentation of a bulk amorphous metal alloy at room temperature. *Science* **295**, 654–657 (2002).

69. T. Rouxel, H. Ji, J. P. Guin, F. Augereau, B. Rufflé, Indentation deformation mechanism in glass: Densification versus shear flow. *J. Appl. Phys.* **107**, 094903 (2010).

70. Z. Q. Chen, M. C. Li, X. Tong, Y. Zhao, J. Y. Xie, S. W. Guo, P. Huang, F. Wang, H. B. Ke, B. A. Sun, W. H. Wang, Hardening and toughening effects of intermediate nanosized structures in a confined amorphous alloy film. *J. Mater. Sci. Technol.* **118**, 44–53 (2022).

71. K. Yan, H. H. Cheng, Y. Liu, H. Liu, S. Q. Fang, J. Bai, Achieving exceptional high ductility in binary Mg-6Zn alloy wire by grain boundary strengthening and twinning-induced plasticity. *Adv. Eng. Mater.* **23**, 2001476 (2021).

72. B. Huang, X. C. Tang, C. Geng, Q. F. He, J. Yi, Q. Wang, W. X. Huang, Q. X. Yuan, Y. Yang, G. Wang, W. H. Wang, Hidden shear bands of diversified structures in a bent heterogeneous metallic glass. *Mater. Sci. Eng. A* **869**, 144726 (2023).

73. Z. Q. Chen, L. Huang, P. Huang, K. W. Xu, F. Wang, T. J. Lu, Clarification on shear transformation zone size and its correlation with plasticity for Zr-based bulk metallic glass in different structural states. *Mater. Sci. Eng. A* **677**, 349–355 (2016).

74. I.-C. Choi, Y. K. Zhao, Y.-J. Kim, B.-G. Yoo, J.-Y. Suh, U. Ramamurty, J.-I. Jang, Indentation size effect and shear transformation zone size in a bulk metallic glass in two different structural states. *Acta Mater.* **60**, 6862–6868 (2012).

75. P. Wen, G. P. Johari, R. J. Wang, W. H. Wang, Change in the vibrational properties of bulk metal glass with time. *Phys. Rev. B* **73**, 224203 (2006).

76. R. S. Miller, R. A. MacPhail, Physical aging in supercooled glycerol: Evidence for heterogeneous dynamics? *J. Phys. Chem. B* **101**, 8635–8641 (1997).

77. N. B. Olsen, J. C. Dyre, T. Christensen, Structural relaxation monitored by instantaneous shear modulus. *Phys. Rev. Lett.* **81**, 1031 (1998).

78. H. S. Chen, The influence of structural relaxation on the density and Young's modulus of metallic glasses. *J. Appl. Phys.* **49**, 3289–3291 (1978).

79. A. Concustell, G. Alcalá, S. Mato, T. G. Woodcock, A. Gebert, J. Eckert, M. D. Baró, Effect of relaxation and primary nanocrystallization on the mechanical properties of Cu$_{60}$Zr$_{22}$Ti$_{18}$ bulk metallic glass. *Intermetallics* **13**, 1214–1219 (2005).

80. G. E. Stong, The modulus of elasticity of glass: I. Preliminary studies: (a) Effect of thermal history; (b) effect of temperature change. *J. Am. Ceram. Soc.* **20**, 16–22 (1937).

81. G. Gavriliu, Effects of added oxide and thermal history on Young's modulus of added oxide (s)-Na$_2$O-SiO$_2$ glass. *Mater. Lett.* **48**, 199–204 (2001).

82. S. Striepe, M. Potuzak, M. M. Smedskjaer, J. Deubener, Relaxation kinetics of the mechanical properties of an aluminosilicate glass. *J. Non Cryst. Solids* **362**, 40–46 (2013).

83. K. L. Kearns, T. Still, G. Fytas, M. D. Ediger, High-modulus organic glasses prepared by physical vapor deposition. *Adv. Mater.* **22**, 39–42 (2010).

84. Q. Du, X. J. Liu, H. Y. Fan, Q. S. Zeng, Y. Wu, H. Wang, D. Chatterjee, Y. Ren, Y. B. Ke, P. M. Voyles, Z. P. Lu, E. Ma, Reentrant glass transition leading to ultrastable metallic glass. *Mater. Today* **34**, 66–77 (2019).

85. H. W. Luan, X. Zhang, H. Y. Ding, F. Zhang, J. H. Luan, Z. B. Jiao, Y.-C. Yang, H. T. Bu, R. B. Wang, J. L. Gu, C. L. Shao, Q. Yu, Y. Shao, Q. S. Zeng, N. Chen, C. T. Liu, K.-F. Yao, High-entropy induced a glass-to-glass transition in a metallic glass. *Nat. Commun.* **13**, 2183 (2022).

86. F. V. Natrup, M. Grofmeier, H. Bracht, Self- and foreign alkaline-earth diffusion in mixed cation silicate glasses. *Solid State Ion.* **180**, 109–115 (2009).

87. T. Maehara, T. Yano, S. Shibata, Structural rules of phase separation in alkali silicate melts analyzed by high-temperature Raman spectroscopy. *J. Non Cryst. Solids* **351**, 3685–3692 (2005).

88. G. V. Afonin, N. P. Kobelev, V. A. Khonik, S. V. Nemilov, Rejuvenation of a metallic and oxide glass by cooling from the supercooled liquid state at laboratory rates. *Phys. Stat. Sol.* **12**, 1800167 (2018).

89. O. A. Hasan, M. C. Boyce, Energy storage during inelastic deformation of glassy polymers. *Polymer* **34**, 5085–5092 (1993).

90. W. C. Oliver, G. M. Pharr, Measurement of hardness and elastic modulus by instrumented indentation: Advances in understanding and refinements to methodology. *J. Mater. Res.* **19**, 3–20 (2004).

91. X. J. Zeng, X. Y. Li, J. Z. Liu, B. Mo, W. Yu, H. Tang, Discerning lunar pyroclastic and impact glasses via Raman spectroscopy. *J. Geophys. Res. Planets* **125**, e2020JE006674 (2020).

92. E. Schreiber, O. L. Anderson, N. Soga, Elastic constants and their measurements (Mcgraw-Hill Education, 1974).

# Science Advances

## Geological timescales' aging effects of lunar glasses

Ziqiang Chen, Yong Zhao, Xiang Chi, Yuqiang Yan, Jie Shen, Minjie Zou, Shaofan Zhao, Ming Liu, Wei Yao, Bo Zhang, Haibo Ke, Xiu-Liang Ma, Haiyang Bai, Mengfei Yang, Zhigang Zou, and Wei-Hua Wang

**View the article online**
https://www.science.org/doi/10.1126/sciadv.adi6086
**Permissions**
https://www.science.org/help/reprints-and-permissions

Use of this article is subject to the Terms of service